

Isostatic constraint for 2D gravity inversion on passive rifted margins

B. Marcela S. Bastos* and Vanderlei C. Oliveira Jr*

**Observatório Nacional,*

Department of Geophysics,

Rio de Janeiro, Brazil

(November 8, 2018)

GEO-XXXX

Running head: **Isostatic constraint for gravity inversion on passive margins**

ABSTRACT

Lorem ipsum dolor sit amet, consectetur adipiscing elit. Ut purus elit, vestibulum ut, placerat ac, adipiscing vitae, felis. Curabitur dictum gravida mauris. Nam arcu libero, nonummy eget, consectetur id, vulputate a, magna. Donec vehicula augue eu neque. Pellentesque habitant morbi tristique senectus et netus et malesuada fames ac turpis egestas. Mauris ut leo. Cras viverra metus rhoncus sem. Nulla et lectus vestibulum urna fringilla ultrices. Phasellus eu tellus sit amet tortor gravida placerat. Integer sapien est, iaculis in, pretium quis, viverra ac, nunc. Praesent eget sem vel leo ultrices bibendum. Aenean faucibus. Morbi dolor nulla, malesuada eu, pulvinar at, mollis ac, nulla. Curabitur auctor semper nulla. Donec varius orci eget risus. Duis nibh mi, congue eu, accumsan eleifend, sagittis quis, diam. Duis eget orci sit amet orci dignissim rutrum.

INTRODUCTION

Several methods have been proposed for using gravity and/or magnetic data to estimate the boundaries of juxtaposed sedimentary layers, the relief of basement and/or the Mohorovicic discontinuity (or simply Moho), which separates crust and mantle. These geophysical discontinuities represent, for such particular methods, density and/or magnetization contrasts in subsurface. All these methods suffer from the inherent ambiguity (Roy, 1962; Skeels, 1947) in determining the true physical property distribution that produces a discrete set of observed potential-field data. It is well known that, by using different density and/or magnetization contrasts, it is possible to find different surfaces producing the same potential-field data. To partially overcome this problem and obtain meaningful solutions, the interpreter must commonly use a priori information obtained from seismic data and/or boreholes in order to constrain the range of possible models.

There are methods that approximate the subsurface by a grid of juxtaposed cells with constant physical property. They estimate the physical property value of each cell and then interpret the estimated values to indirectly estimate the geometry of the geophysical discontinuities. Although very useful in geophysics, such methods are outside the scope of the present work. Here, we consider methods that represent discontinuities by surfaces separating layers with constant or depth-dependent physical property distribution (density and/or magnetization). In this case, the geometry of the geophysical discontinuities are directly determined by estimating the geometrical parameters describing the surfaces.

Different criteria can be used to classify the methods that directly estimate the geometry of geophysical discontinuities. Those applied over a sedimentary basin, for example, can be considered local scale methods, whereas those applied over a continent or country can be

considered regional scale methods and those applied over the whole globe can be considered global scale methods. They can also be classified according to the number of geophysical surfaces to be estimated.

By using these criteria, it is possible to define a first group of methods estimating the geometry of a single interface. In this group, there are local scale methods in space domain (e.g., Bott, 1960; Tanner, 1967; Cordell and Henderson, 1968; Dyrelius and Vogel, 1972; Pedersen, 1977; Pilkington and Crossley, 1986a; Richardson and MacInnes, 1989; Barbosa et al., 1997; Condi et al., 1999; Barbosa et al., 1999b,a; Silva et al., 2006; Pilkington, 2006; Chakravarthi and Sundararajan, 2007; Martins et al., 2010; Silva et al., 2010; Lima et al., 2011; Martins et al., 2011; Barnes and Barraud, 2012; Silva et al., 2014; Silva and Santos, 2017), and Fourier domain (e.g., Oldenburg, 1974; Granser, 1987; Reamer and Ferguson, 1989; Guspí, 1993). Most of these methods were applied to estimate the relief of basement under a sedimentary basin. There are also regional scale methods for estimating a single interface representing the Moho in spaced domain (e.g., Shin et al., 2009; Bagherbandi and Eshagh, 2012; Barzaghi and Biagi, 2014; Sampietro, 2015; Uieda and Barbosa, 2017) and in Fourier domain (e.g., Braitenberg et al., 1997; Braitenberg and Zadro, 1999; van der Meijde et al., 2013). Additionally, there are some global scale methods for estimating the Moho in spaced domain (e.g., Sünkel, 1985; Sjöberg, 2009).

The second group of methods is formed by those estimating multiple surfaces separating layers with constant or depth-dependent physical properties (e.g., Pilkington and Crossley, 1986b; Gallardo et al., 2005; Condi et al., 1999; Camacho et al., 2011; Salem et al., 2014). All these methods have been applied at local scale, to characterize a single sedimentary basin. The number of methods forming this group is significantly lower than that in the first one. Additionally, the methods forming the second group suffer from a greater ambiguity and,

as a consequence, they require more a priori information to decrease the number of possible solutions.

Among those directly estimating the geometry of the surfaces, there are some regional and global scale methods in space domain that impose some degree of isostatic equilibrium to the estimated models (e.g., Süinkel, 1985; Sjöberg, 2009; Bagherbandi and Eshagh, 2012; Sampietro, 2015) or analyze their deviations from a perfect isostatic equilibrium (e.g., Shin et al., 2009). Salem et al. (2014) presented one of the few local scale methods in space domain for simultaneously estimating the basement and Moho reliefs. They impose a perfect isostatic equilibrium according to the Airy’s local compensation model (Turcotte and Schubert, 2002), which describes well the transition from continental to oceanic crust at rifted margins (Worzel, 1968). Their method approximates the subsurface by three juxtaposed layers having constant density contrasts. They are defined in terms of 2D bodies having polygonal cross-sections and represent sediments, crust and mantle. The two interfaces separating them represent the basement and Moho reliefs. In their method, Salem et al. (2014) estimate the basement relief by using an iterative approach similar to that presented by Bott (1960) and Cordell and Henderson (1968). The difference is that, at each iteration, they use the Airy’s model to update the Moho geometry. As properly pointed out by Silva et al. (2014), Bott’s method does not define optimal step sizes at the iterative corrections, does not impose constraints for obtaining stable solutions, nor use an objective stopping criterion. It is reasonable to presume that the method presented by Salem et al. (2014) is also susceptible to these limitations based on its resemblance with that proposed by Bott.

Here, we present a new local scale method for simultaneously estimating the geometries of basement and Moho along a profile on a passive rifted margin. Our method is formulated, in space domain, as a non-linear gravity inversion. In order to produce stable solutions

and introduce a priori information, we use different constraints imposing smoothness and lower/upper bounds on basement and Moho depths, as well as proximity between estimated and known depths at some points along the profile. We also impose isostatic equilibrium to the estimated model. However, differently from previous methods, we introduce this information by imposing smoothness on the lithostatic stress exerted by the interpretation model on a planar surface located at depth, below which we assume that there is no lateral density variations. This constraint, which we conveniently call as *isostatic constraint*, imposes that the lithostatic stress must be smooth along the entire profile, except at some isolated regions, where it can present abrupt variations. At these regions, our method enables the estimated model deviates from the isostatic equilibrium. Consequently, our method does not estimate a model in perfect isostatic equilibrium, but a model as close as possible to the isostatic equilibrium according to the Airy’s local model. Tests with synthetic data show the good performance of our method in simultaneously retrieving the geometry of basement and Moho of a simulated volcanic margin model. Finally, we illustrate an application of our method to invert gravity data provided by the global model EIGEN6C4 (Förste et al., 2014) on a profile over the Pelotas basin (Stica et al., 2014). This basin is located at the southern of Brazil and is considered a classical example of volcanic passive margin (Geoffroy, 2005). We obtained results that are very consistent with a previous interpretation presented by Zalán (2015), which used ultra-deep seismic data. These results show that our method can be very effective at regions presenting abrupt crustal thinning, which is typically shown in volcanic passive margins.

METHODOLOGY

Forward problem

Let \mathbf{d}^o be the observed data vector, whose i -th element d_i^o , $i = 1, \dots, N$, represent the observed gravity disturbance at the point (x_i, y_i, z_i) , on a profile located over a rifted passive margin. The coordinates are referred to a topocentric Cartesian system, with z axis pointing downward, y -axis along the profile and x -axis perpendicular to the profile. We assume that the actual mass distribution in a rifted passive margin can be schematically represented according to Figure 1. In this model, the subsurface is formed by four layers. The first and shallowest one represents a water layer with constant density $\rho^{(w)}$. The second layer is formed by Q vertically adjacent parts representing sediments, salt or volcanic rocks. In our example, this layer is formed by two parts with constant densities $\rho^{(q)}$, $q = 1, 2$. Different models can be created by changing the number Q . The third layer of our model represents the crust. For simplicity, we presume that the crust density assumes two possible values. It can be equal to $\rho^{(cc)}$, which represents the continental crust, or equal to $\rho^{(oc)}$, which represents the oceanic crust. The deepest layer represents a homogeneous mantle with constant density $\rho^{(m)}$. The interface separating the second and third layers defines the basement relief whereas that separating the third and fourth layers defines the Moho. These surfaces are represented by dashed-white lines in Figure 1. We also presume the existence of an isostatic compensation depth at S_0 (represented as a continuous white line in Figure 1), below which there is no lateral variations in the mass distribution.

In order to define the anomalous mass distribution producing the observed gravity disturbance, we presume a reference mass distribution formed by two layers (not shown). The shallowest layer represents a homogeneous crust with constant density $\rho^{(r)}$. The deepest

layer in the reference mass distribution represents a homogeneous mantle with constant density $\rho^{(m)}$. Notice that the mantle in the reference mass distribution has the same density as the mantle in our rifted margin model (Figure 1). The interface separating the crust and mantle in the reference mass distribution is conveniently called *reference Moho* (represented as a continuous white line in Figure 1). The reference model can be thought of as the outer layers of a concentric mass distribution producing the normal gravity field.

We consider that the anomalous mass distribution producing the observed data is defined as the difference between the rifted margin model (Figure 1) and the reference mass distribution (not shown). As a consequence, the anomalous mass distribution is characterized by regions with constant density contrast. This anomalous distribution is approximated by an interpretation model formed by N columns of vertically stacked prisms (Figure 2). For convenience, we presume that there is an observed gravity disturbance over the center of each column. We consider that the prisms in the extremities of the interpretation model extend to infinity along the y axis in order to prevent edge effects in the forward calculations. The i -th column is formed by four vertically adjacent layers, which in turn are composed of vertically adjacent prisms having infinite length along the x -axis.

The first and shallowest layer represents water, is formed by a single prism, has thickness $t_i^{(w)}$ and a constant density contrast $\Delta\rho^{(w)} = \rho^{(w)} - \rho^{(r)}$. The second layer forming the i -th column of the interpretation model is defined by the interpreter, according to the geological environment to be studied and the a priori information availability. As a general rule, this layer can be defined by a set of Q vertically adjacent prisms, each one with thickness $t_i^{(q)}$ and constant density contrast $\Delta\rho^{(q)} = \rho^{(q)} - \rho^{(r)}$, $q = 1, \dots, Q$. The third layer represents the crust, it is also formed by a single prism, has thickness $t_i^{(c)}$ and density contrast $\Delta\rho_i^{(c)} = \rho^{(c)} - \rho^{(r)}$, with ρ^c being the crust density. According to our rifted margin

model (Figure 1), the crust density $\rho_i^{(c)}$ may assume two possible values, depending on its position with respect to the y_{COT} (Figure 2). As a consequence, the prisms forming the third layer of the interpretation model may have two possible density contrasts: $\Delta\rho_i^{(c)} = \rho^{(cc)} - \rho^{(r)}$, for $y_i \leq y_{COT}$, or $\Delta\rho_i^{(c)} = \rho^{(oc)} - \rho^{(r)}$, for $y_i > y_{COT}$. The top of this layer defines the basement relief and its bottom the relief of the Moho. The fourth layer represents the mantle, it is divided into two parts, each one formed by a single prism having a constant density contrast $\Delta\rho^{(m)} = \rho^{(m)} - \rho^{(r)}$. The shallowest portion of this layer has thickness $t_i^{(m)}$. Its top and bottom define, respectively, the depths of Moho and the planar surface at the compensation depth S_0 . The deepest portion of the fourth layer has thickness ΔS_0 , top at the surface S_0 and bottom at the planar surface $S_0 + \Delta S_0$, which defines the reference Moho.

Given the density contrasts, the COT position y_{COT} , the isostatic compensation depth S_0 , the thickness of the water layer and of the $Q - 1$ prisms forming the shallowest portion of the second layer, it is possible to describe the interpretation model in terms of an $M \times 1$ parameter vector \mathbf{p} , $M = 2N + 1$, defined as follows:

$$\mathbf{p} = \begin{bmatrix} \mathbf{t}^Q \\ \mathbf{t}^m \\ \Delta S_0 \end{bmatrix}, \quad (1)$$

where \mathbf{t}^Q and \mathbf{t}^m are $N \times 1$ vectors whose i -th elements t_i^Q and t_i^m represent, respectively, the thickness of the prism forming the deepest portion of the second layer and the thickness of the prism forming the shallowest portion of the fourth layer of the interpretation model. As a consequence, t_i^Q and t_i^m approximate, respectively, the geometry of basement relief and Moho. In this case, the gravity disturbance produced by the interpretation model (the predicted gravity disturbance) at the position (x_i, y_i, z_i) can be written as the sum of

the vertical component of the gravitational attraction exerted by the L prisms forming the interpretation model as follows:

$$d_i(\mathbf{p}) = k_g G \sum_{j=1}^L f_{ij}(\mathbf{p}) , \quad (2)$$

where $f_{ij}(\mathbf{p})$ represents an integral over the volume of the j -th prism. Here, these volume integrals are computed with the expressions proposed by Nagy et al. (2000), by using the open-source Python package *Fatiando a Terra* (Uieda et al., 2013).

Inverse problem formulation

Let $\mathbf{d}(\mathbf{p})$ be the predicted data vector, whose i -th element $d_i(\mathbf{p})$ is the vertical component of the gravitational attraction (equation 2) exerted by the interpretation model at the position (x_i, y_i, z_i) on the profile. Estimating the particular parameter vector producing a predicted data $\mathbf{d}(\mathbf{p})$ as close as possible to the observed data \mathbf{d}^o can be formulated as the problem of minimizing the goal function

$$\Gamma(\mathbf{p}) = \Phi(\mathbf{p}) + \sum_{\ell=0}^3 \alpha_{\ell} \Psi_{\ell}(\mathbf{p}) , \quad (3)$$

subject to the inequality constraint

$$p_j^{min} < p_j < p_j^{max} , \quad j = 1, \dots, M , \quad (4)$$

where p_j^{min} and p_j^{max} define, respectively, lower and upper bounds for the j -th element of \mathbf{p} .

In equation 3, α_{ℓ} is the weight assigned to the ℓ -th regularizing function $\Psi_{\ell}(\mathbf{p})$, $\ell = 0, 1, 2, 3$, and $\Phi(\mathbf{p})$ is the misfit function given by

$$\Phi(\mathbf{p}) = \frac{1}{N} \|\mathbf{d}^o - \mathbf{d}(\mathbf{p})\|_2^2 , \quad (5)$$

where $\|\cdot\|_2^2$ represents the squared Euclidean norm. Details about the regularizing functions $\Psi_{\ell}(\mathbf{p})$, $\ell = 0, 1, 2, 3$ and the numerical procedure to solve this non-linear inverse problem

are given in the following sections.

Isostatic constraint

Consider that no vertical forces are acting on the lateral surfaces of each column forming the model (Figure 2). In this case, the lithostatic stress (pressure) exerted by the i -th column at the surface S_0 can be computed as follows (Turcotte and Schubert, 2002):

$$t_i^{(w)} \rho^{(w)} + t_i^{(1)} \rho_i^{(1)} + \dots + t_i^{(Q)} \rho_i^{(Q)} + t_i^{(c)} \rho_i^{(c)} + t_i^{(m)} \rho^{(m)} = \tau_i, \quad (6)$$

where τ_i is the ratio of lithostatic stress to the mean gravity value on the study area. By rearranging terms in equation 6 and using the relation

$$S_0 = t_i^{(w)} + t_i^{(1)} + \dots + t_i^{(Q)} + t_i^{(c)} + t_i^{(m)}, \quad (7)$$

it is possible to show that:

$$\Delta \tilde{\rho}_i^{(Q)} t_i^{(Q)} + \Delta \tilde{\rho}_i^{(m)} t_i^{(m)} + \Delta \tilde{\rho}_i^{(w)} t_i^{(w)} + \Delta \tilde{\rho}_i^{(1)} t_i^{(1)} + \dots + \Delta \tilde{\rho}_i^{(Q-1)} t_i^{(Q-1)} + \rho_i^{(c)} S_0 = \tau_i, \quad (8)$$

where $\Delta \tilde{\rho}_i^{(\alpha)} = \rho_i^{(\alpha)} - \rho_i^{(c)}$, $\alpha = w, 1, \dots, Q-1, Q, m$. In order to describe the lithostatic stress exerted by all columns forming the interpretation model on the surface S_0 , equation 8 can be written as follows:

$$\mathbf{M}^{(Q)} \mathbf{t}^{(Q)} + \mathbf{M}^{(m)} \mathbf{t}^{(m)} + \mathbf{M}^{(w)} \mathbf{t}^{(w)} + \mathbf{M}^{(1)} \mathbf{t}^{(1)} + \dots + \mathbf{M}^{(Q-1)} \mathbf{t}^{(Q-1)} + \boldsymbol{\rho}^{(c)} S_0 = \boldsymbol{\tau}, \quad (9)$$

where $\boldsymbol{\tau}$ is an $N \times 1$ vector whose i -th element is the τ_i (equation 6) associated with the i -th column, $\mathbf{t}^{(\alpha)}$, $\alpha = w, 1, \dots, Q-1, Q, m$, is a $N \times 1$ vector with i -th element defined by the thickness $t_i^{(\alpha)}$ of a prism in the i -th column, $\mathbf{M}^{(\alpha)}$ is an $N \times N$ diagonal matrix whose elements in the main diagonal are defined by the density contrasts $\Delta \tilde{\rho}_i^{(\alpha)}$, $i = 1, \dots, N$, of the prisms in a layer and $\boldsymbol{\rho}^{(c)}$ is an $N \times 1$ vector containing the densities of the prisms representing the crust.

Let us now consider that the interpretation model is in isostatic equilibrium according to the Airy's local model (e.g., Turcotte and Schubert, 2002; Hofmann-Wellenhof and Moritz, 2005; Lowrie, 2007). In this case, the lithostatic stress exerted by the interpretation model must be constant on a planar surface located at depth. Differently from previous approaches in literature, we impose this condition by applying the first-order Tikhonov regularization (Aster et al., 2005) to the vector $\boldsymbol{\tau}$ (equation 9), obtaining the following expression:

$$\mathbf{R}(\mathbf{C}\mathbf{p} + \mathbf{D}\mathbf{t}) = \mathbf{0}, \quad (10)$$

where $\mathbf{0}$ is a vector with null elements and the remaining terms are given by:

$$\mathbf{C} = \begin{bmatrix} \mathbf{M}^{(Q)} & \mathbf{M}^{(m)} & \mathbf{0} \end{bmatrix}_{N \times M}, \quad (11)$$

$$\mathbf{D} = \begin{bmatrix} \mathbf{M}^{(w)} & \mathbf{M}^{(1)} & \dots & \mathbf{M}^{(Q-1)} & \boldsymbol{\rho}^{(c)} \end{bmatrix}_{N \times (QN+1)}, \quad (12)$$

$$\mathbf{t} = \begin{bmatrix} \mathbf{t}^{(w)} \\ \mathbf{t}^{(1)} \\ \vdots \\ \mathbf{t}^{(Q-1)} \\ S_0 \end{bmatrix}_{(QN+1) \times 1}, \quad (13)$$

and \mathbf{R} is an $(N-1) \times N$ matrix, whose element ij is defined as follows:

$$[\mathbf{R}]_{ij} = \begin{cases} 1 & , \quad j = i \\ -1 & , \quad j = i + 1 \\ 0 & , \quad \text{otherwise} \end{cases} \quad (14)$$

Finally, from equation 10, it is possible to define the regularizing function $\Psi_0(\mathbf{p})$ (equation 3):

$$\Psi_0(\mathbf{p}) = \|\mathbf{W}\mathbf{R}(\mathbf{C}\mathbf{p} + \mathbf{D}\mathbf{t})\|_2^2, \quad (15)$$

where \mathbf{W} is an $(N - 1) \times (N - 1)$ diagonal matrix having constant elements $0 < w_{ii} \leq 1$, $i = 1, \dots, N - 1$. Function $\Psi_0(\mathbf{p})$ defines the *Isostatic constraint*.

Notice that, by minimizing the function $\Psi_0(\mathbf{p})$ (equation 15), the method imposes smoothness on the lithostatic stress exerted by the interpretation model on the compensation depth S_0 . Matrix \mathbf{W} controls the relative amount of isostatic equilibrium imposed along the profile. In the particular case in which all diagonal elements w_{ii} have the same constant value, the same amount of isostatic equilibrium is imposed along the whole profile. On the other hand, different amounts of isostatic equilibrium can be imposed along the profile by varying the values of these elements. Elements $w_{ii} \approx 1$ impose a smooth lithostatic stress curve at the transition between columns i and $i + 1$ of the interpretation model. Elements $w_{ii} \approx 0$ allow abrupt variations in the lithostatic stress curve between columns i and $i + 1$ of the interpretation model. By using all elements $w_{ii} = 1$, we impose full isostatic equilibrium along the entire profile. Alternatively, we may enable the interpretation model deviates from the isostatic equilibrium by conveniently decreasing the numerical values assigned to the elements w_{ii} at specific regions along the profile. The strategy used to define the elements w_{ii} is presented in the specific section describing the numerical solution of the inverse problem.

Smoothness constraint

This constraint imposes smoothness on the adjacent thickness of the prisms forming the deepest portion of the second layer and the shallowest part of the fourth layer of the interpretation model by applying the first-order Tikhonov regularization (Aster et al., 2005) to the vectors $\mathbf{t}^{(Q)}$ and $\mathbf{t}^{(m)}$ (equation 1). Mathematically, this constraint is represented by

the regularizing function $\Psi_1(\mathbf{p})$ (equation 3):

$$\Psi_1(\mathbf{p}) = \|\mathbf{S}\mathbf{p}\|_2^2, \quad (16)$$

where \mathbf{S} is an $2(N-1) \times M$ matrix given by:

$$\mathbf{S} = \begin{bmatrix} \mathbf{R} & \mathbf{0} & \mathbf{0} \\ \mathbf{0} & \mathbf{R} & \mathbf{0} \end{bmatrix}, \quad (17)$$

where \mathbf{R} is defined by equation 14 and $\mathbf{0}$ are matrices with all elements equal to zero.

Equality constraint

Equality constraint on vector \mathbf{t}^Q

Let \mathbf{a} be a vector whose k -th element a_k , $k = 1, \dots, A$, is the difference between a known basement depth and the sum of the thickness of the upper portions of the interpretation model (water layer and the upper parts of second layer), all at the same horizontal coordinate y_k^A of the profile. These differences, which must be positive, are used to define the regularizing function $\Psi_2(\mathbf{p})$ (equation 3):

$$\Psi_2(\mathbf{p}) = \|\mathbf{A}\mathbf{p} - \mathbf{a}\|_2^2, \quad (18)$$

where \mathbf{A} is an $A \times M$ matrix whose k -th line has one element equal to one and all the remaining elements equal to zero. The location of the single non-null element in the k -th line of \mathbf{A} depends on the coordinate y_k^A of the known basement depth a_k . Let us consider, for example, an interpretation model formed by $N = 10$ columns. Consider also that the thickness of the deepest part Q of the second layer forming the interpretation model at the coordinates $y_1^A = y_4$ and $y_2^A = y_9$ are equal to 25 and 35.7 km, respectively. In this case, $A = 2$, \mathbf{a} is a 2×1 vector with elements $a_1 = 25$ and $a_2 = 35.7$ and \mathbf{A} is a $2 \times M$ matrix

($M = 2N + 1 = 21$). The element 4 of the first line and the element 9 of the second line of \mathbf{A} are equal to 1 and all its remaining elements are equal to zero.

Equality constraint on vector \mathbf{t}^m

Let \mathbf{b} be a vector whose k -th element b_k , $k = 1, \dots, B$, is the difference between the isostatic compensation depth S_0 and the known Moho depth at the horizontal coordinate y_k^B of the profile. These differences, which must be positive, define known thickness values of the upper part of the fourth layer forming the interpretation model. These values are used to define the regularizing function $\Psi_3(\mathbf{p})$ (equation 3):

$$\Psi_3(\mathbf{p}) = \|\mathbf{B}\mathbf{p} - \mathbf{b}\|_2^2, \quad (19)$$

where \mathbf{B} is a $B \times M$ matrix whose k -th line has one element equal to one and all the remaining elements equal to zero. This matrix is defined in the same way as matrix \mathbf{A} (equation 18).

Computational procedures for solving of the inverse problem

The parameter vector \mathbf{p} (equation 1) minimizing the goal function $\Gamma(\mathbf{p})$ (equation 3), subjected to the inequality constraint (equation 4), is estimated in three steps. At each step, the goal function is minimized by using the Levenberg-Marquardt method (Aster et al., 2005) and the inequality constraint (equation 4) is incorporated by using the same strategy employed by Barbosa et al. (1999b). All derivatives of the misfit function $\Phi(\mathbf{p})$ (equation 5) with respect to the parameters are computed by using a finite difference approximation.

The first step consists in solving the inverse problem without imposing the isostatic constraint, by using $\alpha_0 = 0$ (equation 3). For this step, the interpreter must set:

- Parameters defining the interpretation model (Figure 2): density contrasts $\Delta\rho^{(\alpha)}$, $\alpha = w, 1, \dots, Q, cc, oc, m$, of the four layers, COT position y_{COT} and isostatic compensation depth S_0 . Figure 2 illustrates the case in which the second layer is formed by $Q = 2$ parts. This number, however, can be changed according to the study area.
- Parameters for the inversion: weights α_ℓ , $\ell = 1, 2, 3$ (equation 3), associated to the smoothness and equality constraints (equations 16, 18 and 19), lower and upper bounds p_j^{min} and p_j^{max} (equation 4), $j = 1, \dots, M$, for the parameters to be estimated, vectors **a** (equation 18) and **b** (equation 19) containing known thickness values and an initial approximation $\mathbf{p}^{(0)}$ for the parameter vector **p** (equation 1). The initial approximation $\mathbf{p}^{(0)}$ must satisfy the inequality constraints (equation 4).

The estimated parameter vector obtained at the end of this first step is conveniently called $\mathbf{p}^{(1)}$. The main goal in this step is finding suitable values for the parameters defining the interpretation model and those used for inversion. Several trials may be necessary to find suitable values for these parameters.

The second step consists in obtaining an estimated parameter vector $\mathbf{p}^{(2)}$ by imposing full isostatic equilibrium on the interpretation model along the entire profile. In this step, the interpreter must use the same initial approximation $\mathbf{p}^{(0)}$ for the parameter vector **p** (equation 1). Additionally, the interpreter must find a suitable value for the weight $\alpha_0 = 0$ (equation 3) controlling the isostatic constraint, by using the matrix **W** (equation 15) equal to the identity. We presume that, by imposing full isostatic equilibrium along the entire profile, the estimated parameter vector $\mathbf{p}^{(2)}$ will produce a good data fit, except at some isolated regions, where there will be large residuals between the observed and predicted data. We assume that, at these regions, the study area deviates from the isostatic equilibrium

described by the Airy's local model.

Finally, the third step consists in obtaining an estimated parameter vector $\mathbf{p}^{(3)}$ by imposing different amounts of isostatic equilibrium on the interpretation model along the entire profile. At this step, the interpreter must compute the diagonal elements w_{ii} of the matrix \mathbf{W} (equation 15) that enable the interpretation model deviates from the isostatic equilibrium at the regions presenting large residuals. The elements of \mathbf{W} are computed as follows:

$$w_{ii} = \exp \left[-\frac{\left(r_i^{(2)} + r_{i+1}^{(2)} \right)^2}{4\sigma} \right], \quad (20)$$

where σ is a positive constant, $\mathbf{p}^{(2)}$ is the estimate parameter vector obtained in the previous step and the variables $r_i^{(2)} = d_i^o - d_i(\mathbf{p}^{(2)})$ and $r_{i+1}^{(2)} = d_{i+1}^o - d_{i+1}(\mathbf{p}^{(2)})$ represent, respectively, the residuals between observed and predicted data (equation 2) at the positions (x_i, y_i, z_i) and $(x_{i+1}, y_{i+1}, z_{i+1})$. Equation 20 defines elements w_{ii} in the interval $]0, 1]$. Additionally, it results in $w_{ii} \approx 1$ at regions where the residuals are close to zero and $w_{ii} \approx 0$ at regions presenting large residuals. The positive constant σ controls the deviation from isostatic equilibrium. Large σ values allow small deviations from isostatic equilibrium at regions presenting large residuals. This strategy to define the elements of matrix \mathbf{W} (equation 15) presumes that the isostatic constraint may produce large residuals at some regions along the profile. To counteract this problem, our method enables the interpretation model deviates from isostatic equilibrium at these regions. This idea is in perfect agreement with the fact that the isostatic equilibrium in a continental margin cannot be perfectly explained by using the Airy's local model.

Other important aspect of our method is related to the values attributed to the weights α_ℓ (equation 3). Their values can be very dependent on the particular characteristics of

the interpretation model and there is no analytical rule to define them. To overcome this problem, we normalize the α_ℓ values as follows:

$$\alpha_\ell = \tilde{\alpha}_\ell \frac{E_\Phi}{E_\ell}, \quad \ell = 0, 1, 2, 3, \quad (21)$$

where $\tilde{\alpha}_\ell$ is a positive scalar and E_Φ/E_ℓ is a normalizing constant. In this equation, E_ℓ represents the median of the elements forming the main diagonal of the Hessian matrix of the ℓ -th constraining function $\Psi_\ell(\mathbf{p})$ (equations 15, 16, 18 and 19). The constant E_Φ is defined in a similar way by using the Hessian matrix of the misfit function $\Phi(\mathbf{p})$ (equation 5) computed with the initial approximation $\mathbf{p}^{(0)}$ for the parameter vector \mathbf{p} (equation 1) at the first step. According to this empirical strategy, the weights α_ℓ are defined by using the positive scalars $\tilde{\alpha}_\ell$ (equation 21), which are less dependent on the particular characteristics of the interpretation model.

The algorithm can be summarized as follows:

- (Step 1)** Use $\tilde{\alpha}_0 = 0$ and set non-null values for $\tilde{\alpha}_1$, $\tilde{\alpha}_2$ and $\tilde{\alpha}_3$ (equation 21). Define p_j^{min} , p_j^{max} (equation 4), \mathbf{a} (equation 18) and \mathbf{b} (equation 19). Define an initial approximation $\mathbf{p}^{(0)}$ satisfying the inequality constraint (equation 4). Use $\mathbf{p}^{(0)}$ to compute the Hessian matrix of the misfit function $\Phi(\mathbf{p})$ (equation 5). Compute the Hessian matrices of the constraining functions $\Psi_\ell(\mathbf{p})$, $\ell = 1, 2, 3$ (equations 16, 18 and 19). Compute E_Φ , E_ℓ and α_ℓ (equation 21), $\ell = 1, 2, 3$. Estimate a parameter vector $\mathbf{p}^{(1)}$ minimizing $\Gamma(\mathbf{p})$ (equation 3), subject to the inequality constraint (equation 4).
- (Step 2)** Use the same initial approximation $\mathbf{p}^{(0)}$ of the previous step. Set \mathbf{W} (equation 15) equal to identity. Set a non-null value for $\tilde{\alpha}_0$ (equation 21). Compute the Hessian matrix of the constraining function $\Psi_0(\mathbf{p})$ (equation 15). Compute E_0 and α_0 (equa-

tion 21). Estimate a parameter vector $\mathbf{p}^{(2)}$ minimizing $\Gamma(\mathbf{p})$ (equation 3), subject to the inequality constraint (equation 4).

(Step 3) Use $\mathbf{p}^{(2)}$ as initial approximation. Set the positive constant σ and compute the diagonal elements w_{ii} (equation 20), $i = 1, \dots, N - 1$. With the new \mathbf{W} , compute the Hessian matrix of the constraining function $\Psi_0(\mathbf{p})$ (equation 15). Estimate a parameter vector $\mathbf{p}^{(3)}$ minimizing $\Gamma(\mathbf{p})$ (equation 3), subject to the inequality constraint (equation 4).

APPLICATIONS TO SYNTHETIC DATA

We have simulated a simple volcanic margin model formed by four layers: water, sediments + seaward dipping reflectors, crust (continental and oceanic) and mantle. Parameters defining this model are shown in Table 1. By following the algorithm described in the previous section, we applied our method to invert the synthetic gravity disturbance data produced by our volcanic margin model.

Figure 3 shows the results obtained at Step 1 of our algorithm. The interpretation model was defined by using the parameters shown in Table 1. The parameters $\tilde{\alpha}_1$, $\tilde{\alpha}_2$ and $\tilde{\alpha}_3$ (equation 21) used to estimate a parameter vector $\mathbf{p}^{(1)}$ without imposing the isostatic constraint have values 10^1 , 10^1 and 10^2 , respectively. As we can see, the estimated model produces a gravity disturbance and a lithostatic stress very close to the simulated ones and the estimated Moho retrieves the true one. On the other hand, the estimated basement relief is very smooth and does not retrieve the true one along the first 200 km of the profile.

Figure 4 shows the estimated model obtained at the end of Step 2, by using $\tilde{\alpha}_0 = 10^2$ (equation 21). In comparison to the estimated model obtained in the Step 1 (Figure 3),

this result shows a very smooth lithostatic stress curve as a consequence of the isostatic constraint. The use of the isostatic constraint has produced a worse estimated Moho, but has improved the estimated basement relief. The main improvement occurs along the first ≈ 100 km on the profile, where the true model exhibits a pronounced crustal thinning. The region between approximately 100 and 200 km, however, shows large differences between the estimated and true basement reliefs. At this region, we can also notice the presence of large differences between the simulated and predicted gravity disturbances.

Figure 5 shows the estimated model obtained at the Step 3 of our algorithm, by using $\sigma = 21$ (equation 20). In comparison with the estimated model obtained at Step 2 (Figure 4), the new estimated model produces a very good data fit along the whole profile. Additionally, it shows an estimated Moho that, regardless of the small artifact created at the position ≈ 150 km, is closer to the true one. The estimated basement relief is worse than that obtained at Step 2 (Figure 4), but it is still much better than that obtained at Step 1 (Figure 3). It worth noting that the new lithostatic stress curve contains an abrupt variation at the region located between 100 and 200 km, showing that our method was able to successfully enables the interpretation model deviates from the isostatic equilibrium at an isolated region. This region coincides with that presenting the large absolute differences between the gravity disturbance data in Figure 4.

The estimated model obtained at Step 3 (Figure 5) by using the isostatic constraint is superior than that obtained at Step 1 (Figure 3), without using the isostatic constraint. It is possible to obtain a good estimated model without using the isostatic constraint, but it requires a great number of known depths along the profile. This can be verified by comparing the estimated models shown in Figures 6 and 7. The first one shows an estimated model obtained in the same way as that shown in Figure 3, but by using a great number of

additional known depths at basement. As we can see, the additional known depths improve the estimated basement relief. In practical situations, however, the amount of available a priori information on the study area is limited. Figure 7 shows an estimated model obtained in the same way as that shown in Figure 5, but by using a limited number of additional known depths at basement. Notice that the number of additional known depths is smaller than that used in Figure 6. Other curious feature noted in this new model is that, similarly to that shown in Figure 5, the estimated Moho shows an artifact at the position ≈ 150 km. Notwithstanding this artifact, this result shows that the isostatic constraint can be very effective in retrieving the basement relief and Moho by using a limited amount of a priori information.

APPLICATION TO REAL DATA

We applied our method to interpret a gravity profile over the Pelotas basin (Stica et al., 2014), located at the southern of Brazil. This basin is considered a classical example of volcanic margin (Geoffroy, 2005). We apply our method to the gravity disturbance data provided by the EIGEN6C4 model (Förste et al., 2014) on the study area.

Figure 8 shows the estimated model obtained at the Step 3 of our algorithm, by using $\sigma = 58$ (equation 20), $\tilde{\alpha}_0 = 10^2$, $\tilde{\alpha}_1 = 10^1$, $\tilde{\alpha}_2 = 10^1$ and $\tilde{\alpha}_3 = 10^2$ (equation 21). Parameters defining the interpretation model are the same used to define our volcanic margin model (Table 1). The initial approximation used in Steps 1 and 2 (not shown) was obtained by interpreting a seismic section presented by Stica et al. (2014). As we can see, the estimated model produces a very good data fit along the whole profile. Our estimated model is very close to that obtained independently by Zalán (2015). The larger differences (≈ 10 km) occur at the basement, along the first 100 km of the profile. At this region, Zalán proposes

a steep variation in basement relief, which shows a maximum depth ≈ 30 km. On the other hand, our result shows a smooth variation in basement relief. Despite these large differences, Figure 8 shows that our model produces a very good data fit at this region. It means that, by presuming an SDR having a small density contrast (Table 1), the steep variation proposed by Zalán in the basement relief cannot be determined by using only gravity data. It worth noting that the estimated lithostatic stress curve contains abrupt variations at an isolated region close to 150 km, indicating deviations of our estimated model from the isostatic equilibrium predicted by the Airy’s local model. On the remaining parts of the profile, the lithostatic stress curve is very smooth, suggesting that the Pelotas basin is in isostatic equilibrium according to the Airy’s model on those regions.

Figure 9 shows an estimated model obtained in the same way as that shown in Figure 8, but by using additional known depths at basement. Similarly to that shown in Figure 8, the new model (Figure 9) produces a very good data fit and deviates from the isostatic equilibrium at the position ≈ 150 km. Notice that, by using the additional known depths, the differences between our model and that obtained by Zalán (2015) decrease considerably without producing significant changes in the predicted data. It is worth stressing that our results were obtained by using gravity data provided by the global gravity model EIGEN6C4 (Förste et al., 2014), whereas Zalán (2015) obtained his result by interpreting ultra-deep seismic sections available to the petroleum industry.

CONCLUSIONS

We present a new local scale method for simultaneously estimating the geometries of basement and Moho on a profile located on a passive rifted margin. Our method approximates the subsurface by a set of adjacent columns, each one divided into four layers. The first

one represents water; the second is formed by vertically stacked parts, according to the complexity of the study area; the third and fourth represent, respectively, the crust and mantle, being the last one formed by two vertically stacked parts. The interface separating the upper and lower parts of the fourth layer represents a planar surface below which there is no lateral density variations. This planar surface defines the isostatic compensation depth. The interfaces defining the top and bottom of the third layer define, respectively, the basement and Moho in our model. We assume that the Crust-Ocean Transition (COT) can be represented by an abrupt and vertical interface. The layers representing water and mantle have constant density contrasts. In the second layer, each part has a constant density contrast. The density contrast in the third layer assumes two possible values representing the continental crust, before the COT, and oceanic crust, after the COT.

Our method presumes the knowledge of the COT position, the compensation depth, all density contrasts and the geometry of all layers above the basement. The method is formulated as a non-linear inverse problem. The parameters to be estimated are the thickness of the deeper part forming the second layer, the thickness of the upper part forming the fourth layer and the constant thickness of the deeper part forming the fourth layer. Because all parameters represent thickness, we force them to be positive. In order to obtain stable solutions, we impose the estimated basement and Moho to be smooth and close to some points having known depths along the profile. We also impose isostatic equilibrium according to the Airy’s local compensation model. Our original approach introduces this information by enforcing that the lithostatic stress exerted by the model on a planar surface located at the compensation depth must be mostly smooth, except at some isolated regions, where it can present abrupt variations.

Tests with synthetic data show that the isostatic constraint can considerably improve

the estimated model at regions showing pronounced crustal thinning, which are typical of volcanic passive margins. Applications to real data over the Pelotas basin, considered a classical volcanic margin at the southern of Brazil, produced results in agreement with a previous interpretation obtained independently by using ultra-deep seismic data. These results show that our method can be a useful tool for interpreting gravity data on rifted margins. Further research could be conducted to generalize our method to estimate three dimensional models and also include lateral density variations in mantle and crust.

ACKNOWLEDGMENTS

Lorem ipsum dolor sit amet, consectetur adipiscing elit. Ut purus elit, vestibulum ut, placerat ac, adipiscing vitae, felis. Curabitur dictum gravida mauris. Nam arcu libero, nonummy eget, consectetur id, vulputate a, magna. Donec vehicula augue eu neque. Pellentesque habitant morbi tristique senectus et netus et malesuada fames ac turpis egestas. Mauris ut leo. Cras viverra metus rhoncus sem. Nulla et lectus vestibulum urna fringilla ultrices. Phasellus eu tellus sit amet tortor gravida placerat. Integer sapien est, iaculis in, pretium quis, viverra ac, nunc. Praesent eget sem vel leo ultrices bibendum. Aenean faucibus. Morbi dolor nulla, malesuada eu, pulvinar at, mollis ac, nulla. Curabitur auctor semper nulla. Donec varius orci eget risus. Duis nibh mi, congue eu, accumsan eleifend, sagittis quis, diam. Duis eget orci sit amet orci dignissim rutrum.

REFERENCES

- Aster, R. C., B. Borchers, and C. H. Thurber, 2005, Parameter estimation and inverse problems (international geophysics): Academic Press.
- Bagherbandi, M., and M. Eshagh, 2012, Crustal thickness recovery using an isostatic model and goce data: *Earth, Planets and Space*, **64**, 1053–1057.
- Barbosa, V. C. F., J. ao B. C. Silva, and W. E. Medeiros, 1997, Gravity inversion of basement relief using approximate equality constraints on depths: *Geophysics*, **62**, 1745–1757.
- Barbosa, V. C. F., J. B. C. Silva, and W. E. Medeiros, 1999a, Gravity inversion of a discontinuous relief stabilized by weighted smoothness constraints on depth: *GEOPHYSICS*, **64**, 1429–1437.
- , 1999b, Stable inversion of gravity anomalies of sedimentary basins with nonsmooth basement reliefs and arbitrary density contrast variations: *GEOPHYSICS*, **64**, 754–764.
- Barnes, G., and J. Barraud, 2012, Imaging geologic surfaces by inverting gravity gradient data with depth horizons: *Geophysics*, **77**, G1–G11.
- Barzaghi, R., and L. Biagi, 2014, The collocation approach to Moho estimate: *Annals of Geophysics*.
- Bott, M. H. P., 1960, The use of rapid digital computing methods for direct gravity interpretation of sedimentary basins: *Geophysical Journal International*, **3**, 63–67.
- Braitenberg, C., F. Pettenati, and M. Zadro, 1997, Spectral and classical methods in the evaluation of moho undulations from gravity data: The ne italian alps and isostasy: *Journal of Geodynamics*, **23**, 5 – 22.
- Braitenberg, C., and M. Zadro, 1999, Iterative 3d gravity inversion with integration of seismologic data: *Bollettino di Geofisica Teorica ed Applicata*, **40**, 469–475.
- Camacho, A. G., J. Fernndez, and J. Gottsmann, 2011, A new gravity inversion method for

- multiple subhorizontal discontinuity interfaces and shallow basins: *Journal of Geophysical Research: Solid Earth*, **116**.
- Chakravarthi, V., and N. Sundararajan, 2007, 3d gravity inversion of basement relief a depth-dependent density approach: *GEOPHYSICS*, **72**, I23–I32.
- Condi, F. J., C. A. Zelt, D. S. Sawyer, and G. J. Hirasaki, 1999, Gravity inversion for rifted margin deep structure using extension and isostatic constraints: *Geophysical Journal International*, **138**, 435–446.
- Cordell, L., and R. G. Henderson, 1968, Iterative three-dimensional solution of gravity anomaly data using a digital computer: *GEOPHYSICS*, **33**, 596–601.
- Dyrelus, D., and A. Vogel, 1972, Improvement of convergency in iterative gravity interpretation: *Geophysical Journal of the Royal Astronomical Society*, **27**, 195–205.
- Förste, C., S. Bruinsma, O. Abrikosov, J.-M. Lemoine, J. C. Marty, F. Flechtner, G. Balmino, F. Barthelmes, and R. Biancale, 2014, EIGEN-6C4 The latest combined global gravity field model including GOCE data up to degree and order 2190 of GFZ Potsdam and GRGS Toulouse: <https://doi.org/10.5880/icgem.2015.1>.
- Gallardo, L. A., M. Pérez-Flores, and E. Gómez-Treviño, 2005, Refinement of three-dimensional multilayer models of basins and crustal environments by inversion of gravity and magnetic data: *Tectonophysics*, **397**, 37 – 54. (Integration of Geophysical and Geological Data and Numerical Models in Basins).
- Geoffroy, L., 2005, Volcanic passive margins: *Comptes Rendus Geoscience*, **337**, 1395 – 1408.
- Granser, H., 1987, Three-dimensional interpretation of gravity data from sedimentary basins using an exponential density-depth function: *Geophysical Prospecting*, **35**, 1030–1041.
- Guspi, F., 1993, Noniterative nonlinear gravity inversion: *Geophysics*, **58**, 935–940.

- Hofmann-Wellenhof, B., and H. Moritz, 2005, *Physical geodesy*: Springer.
- Lima, W. A., C. M. Martins, J. B. Silva, and V. C. Barbosa, 2011, Total variation regularization for depth-to-basement estimate: Part 2 physico-geologic meaning and comparisons with previous inversion methods: *Geophysics*, **76**, I13–I20.
- Lowrie, W., 2007, *Fundamentals of geophysics*: Cambridge University Press. (A second edition of this classic textbook on fundamental principles of geophysics for geoscience undergraduates.).
- Martins, C. M., V. C. Barbosa, and J. B. Silva, 2010, Simultaneous 3d depth-to-basement and density-contrast estimates using gravity data and depth control at few points: *GEOPHYSICS*, **75**, I21–I28.
- Martins, C. M., W. A. Lima, V. C. Barbosa, and J. B. Silva, 2011, Total variation regularization for depth-to-basement estimate: Part 1 - mathematical details and applications: *Geophysics*, **76**, I1–I12.
- Nagy, D., G. Papp, and J. Benedek, 2000, The gravitational potential and its derivatives for the prism: *Journal of Geodesy*, **74**, 311–326.
- Oldenburg, D. W., 1974, The inversion and interpretation of gravity anomalies: *Geophysics*, **39**, 526–536.
- Pedersen, L. B., 1977, Interpretation of potential field data a generalized inverse approach: *Geophysical Prospecting*, **25**, 199–230.
- Pilkington, M., 2006, Joint inversion of gravity and magnetic data for two-layer models: *GEOPHYSICS*, **71**, L35–L42.
- Pilkington, M., and D. J. Crossley, 1986a, Determination of crustal interface topography from potential fields: *GEOPHYSICS*, **51**, 1277–1284.
- , 1986b, Inversion of aeromagnetic data for multilayered crustal models: *GEO-*

- PHYSICS, **51**, 2250–2254.
- Reamer, S. K., and J. F. Ferguson, 1989, Regularized twodimensional fourier gravity inversion method with application to the silent canyon caldera, nevada: *Geophysics*, **54**, 486–496.
- Richardson, R. M., and S. C. MacInnes, 1989, The inversion of gravity data into three-dimensional polyhedral models: *Journal of Geophysical Research: Solid Earth*, **94**, 7555–7562.
- Roy, A., 1962, Ambiguity in geophysical interpretation: *Geophysics*, **27**, 90–99.
- Salem, A., C. Green, M. Stewart, and D. D. Lerma, 2014, Inversion of gravity data with isostatic constraints: *GEOPHYSICS*, **79**, A45–A50.
- Sampietro, D., 2015, Geological units and moho depth determination in the western balkans exploiting goce data: *Geophysical Journal International*, **202**, 1054–1063.
- Shin, Y. H., C.-K. Shum, C. Braitenberg, S. M. Lee, H. Xu, K. S. Choi, J. H. Baek, and J. U. Park, 2009, Three-dimensional fold structure of the tibetan moho from grace gravity data: *Geophysical Research Letters*, **36**.
- Silva, J. B., D. C. Costa, and V. C. Barbosa, 2006, Gravity inversion of basement relief and estimation of density contrast variation with depth: *GEOPHYSICS*, **71**, J51–J58.
- Silva, J. B., A. S. Oliveira, and V. C. Barbosa, 2010, Gravity inversion of 2d basement relief using entropic regularization: *Geophysics*, **75**, I29–I35.
- Silva, J. B. C., and D. F. Santos, 2017, Efficient gravity inversion of basement relief using a versatile modeling algorithm: *GEOPHYSICS*, **82**, G23–G34.
- Silva, J. B. C., D. F. Santos, and K. P. Gomes, 2014, Fast gravity inversion of basement relief: *Geophysics*, **79**, G79–G91.
- Sjöberg, L. E., 2009, Solving vening meinesz-moritz inverse problem in isostasy: *Geophysical*

- Journal International, **179**, 1527–1536.
- Skeels, D. C., 1947, Ambiguity in gravity interpretation: *Geophysics*, **12**, 43–56.
- Stica, J. M., P. V. Zalán, and A. L. Ferrari, 2014, The evolution of rifting on the volcanic margin of the pelotas basin and the contextualization of the paranetendeka lip in the separation of gondwana in the south atlantic: *Marine and Petroleum Geology*, **50**, 1 – 21.
- Sünkel, H., 1985, An isostatic Earth model: Scientific report 367, Department of Geodetic Science and Surveying, The Ohio State University, Columbus, Ohio.
- Tanner, J. G., 1967, An automated method of gravity interpretation: *Geophysical Journal of the Royal Astronomical Society*, **13**, 339–347.
- Turcotte, D. L., and G. Schubert, 2002, *Geodynamics*, 2. ed. ed.: Cambridge Univ. Press.
- Uieda, L., and V. C. Barbosa, 2017, Fast nonlinear gravity inversion in spherical coordinates with application to the south american moho: *Geophysical Journal International*, **208**, 162–176.
- Uieda, L., V. C. Oliveira Jr., and V. C. F. Barbosa, 2013, Modeling the earth with fatiando a terra: Proceedings of the 12th Python in Science Conference, 96 – 103.
- van der Meijde, M., J. Julià, and M. Assumpção, 2013, Gravity derived moho for south america: *Tectonophysics*, **609**, 456 – 467. (Moho: 100 years after Andrija Mohorovicic).
- Watts, A. B., and J. D. P. Moore, 2017, Flexural isostasy: Constraints from gravity and topography power spectra: *Journal of Geophysical Research: Solid Earth*, **122**, 8417–8430.
- Worzel, J. L., 1968, Advances in marine geophysical research of continental margins: *Canadian Journal of Earth Sciences*, **5**, 963–983.
- Zalán, P. V., 2015, Similarities and differences between magma-poor and volcanic passive

margins applications to the brazilian marginal basins: 14th International Congress of the
Brazilian Geophysical Society & EXPOGEF, Rio de Janeiro, Brazil, 3-6 August 2015,
37–42.

LIST OF TABLES

1 Properties of the volcanic magin model. The model extends from $y = 0$ km to $y = 383$ km, the Crust-Ocean Transition (COT) is located at $y_{COT} = 350$ km and the reference Moho is located at $S_0 + \Delta S = 43\,200$ km, where $\Delta S = 2\,200$ km (Figures 1 and 2). The density contrasts $\Delta\rho^{(\alpha)}$ are defined with respect to the reference value $\rho^{(r)} = 2870$ kg/m³, which coincides with the density $\rho^{(cc)}$ attributed to the continental crust.

LIST OF FIGURES

1 Rifted margin model formed by four layers. The first one represents a water layer with constant density $\rho^{(w)}$. The second layer is formed by Q vertically adjacent parts, according to the geological are to be studied. In this example, $Q = 2$. These parts represent sediments, salt or volcanic rocks and have constant densities $\rho^{(q)}$, $q = 1, \dots, Q$. The third layer represents the crust, which is divided into the continental crust, with a constant density $\rho^{(cc)}$, and the oceanic crust, with a constant density $\rho^{(oc)}$. We presume an abrupt Crust-Ocean Transition (COT). Finally, the fourth layer of our model represents a homogeneous mantle with constant density $\rho^{(m)}$. Basement and Moho are represented by the dashed-white lines. The continuous white lines represent the isostatic compensation depth at S_0 and the reference Moho at $S_0 + \Delta S$.

2 Interpretation model formed by N columns of vertically stacked prisms. Each column is formed by four layers of prisms and locally approximates the four layers of the rifted margin model (Figure 1). Each prism has a constant density contrast defined as the difference between its corresponding density at the rifted margin model (Figure 1) and the constant density $\rho^{(r)}$ of the shallowest layer forming the reference density distribution (see text). Basement and Moho are represented by the dashed-white lines. The continuous white line represents the isostatic compensation depth at S_0 . The base of the interpretation model coincides with the reference Moho located at $S_0 + \Delta S$.

3 Application to synthetic data. Results obtained in Step 1. (Bottom panel) Estimated and true surfaces, the initial basement and Moho used in the inversion, as well as the known depths at basement and Moho. (Middle panel) True and estimated lithostatic stress curves computed by using equation 6. The values are multiplied by a constant gravity value equal to 9.81 m/s^2 . (Upper panel) True gravity disturbance data produced by the volcanic

margin model (simulated data), data produced by the estimated model (predicted data) and data produced the by model used as initial guess in the inversion (initial guess data). The contour of the prisms forming the interpretation model were omitted. The density contrasts were defined according to Table 1.

4 Application to synthetic data. Results obtained in Step 2. The remaining informations are the same shown in the caption of Figure 3.

5 Application to synthetic data. Results obtained in Step 3 by using $\sigma = 21$ (equation 20). The remaining informations are the same shown in the caption of Figure 3.

6 Application to synthetic data. Results obtained in Step 1 by using additional known depths at basement (purple symbols). The remaining informations are the same shown in the caption of Figure 3.

7 Application to synthetic data. Results obtained in Step 3 by using $\sigma = 21$ (equation 20) and additional known depths at basement (purple symbols). The remaining informations are the same shown in the caption of Figure 3. Notice that, in comparison with the estimated model shown in Figure 6, the number of additional known depths is small.

8 Application to real data on Pelotas basin, Brazil. Results obtained in Step 3 by using $\sigma = 58$ (equation 20). (Bottom panel) Estimated surfaces, initial basement and Moho used in the inversion, as well as the known depths at basement and Moho. The dashed white lines represent an alternative interpretation obtained by Zalán (2015) at the same study area. (Middle panel) Estimated lithostatic stress curve computed by using equation 6. The values are multiplied by a constant gravity value equal to 9.81 m/s^2 . (Upper panel) Observed gravity disturbance data, data produced by the estimated model (predicted data) and data produced the by model used as initial guess in the inversion (initial guess data). The contour of the prisms forming the interpretation model were omitted. The density

contrasts were defined according to Table 1.

9 Application to real data on Pelotas basin, Brazil. Results obtained in Step 3 by using $\sigma = 58$ (equation 20) and additional known depths at basement. The remaining informations are the same shown in the caption of Figure 8.

Geological meaning	$\rho^{(\alpha)}$ (kg/m ³)	$\Delta\rho^{(\alpha)}$ (kg/m ³)	α
water	1030	−1840	w
sediments	2350	−520	1
SDR	2855	−15	2
continental crust	2870	0	cc
oceanic crust	2885	15	oc
mantle	3240	370	m

Table 1: Properties of the volcanic margin model. The model extends from $y = 0$ km to $y = 383$ km, the Crust-Ocean Transition (COT) is located at $y_{COT} = 350$ km and the reference Moho is located at $S_0 + \Delta S = 43\,200$ km, where $\Delta S = 2\,200$ km (Figures 1 and 2). The density contrasts $\Delta\rho^{(\alpha)}$ are defined with respect to the reference value $\rho^{(r)} = 2870$ kg/m³, which coincides with the density $\rho^{(cc)}$ attributed to the continental crust.

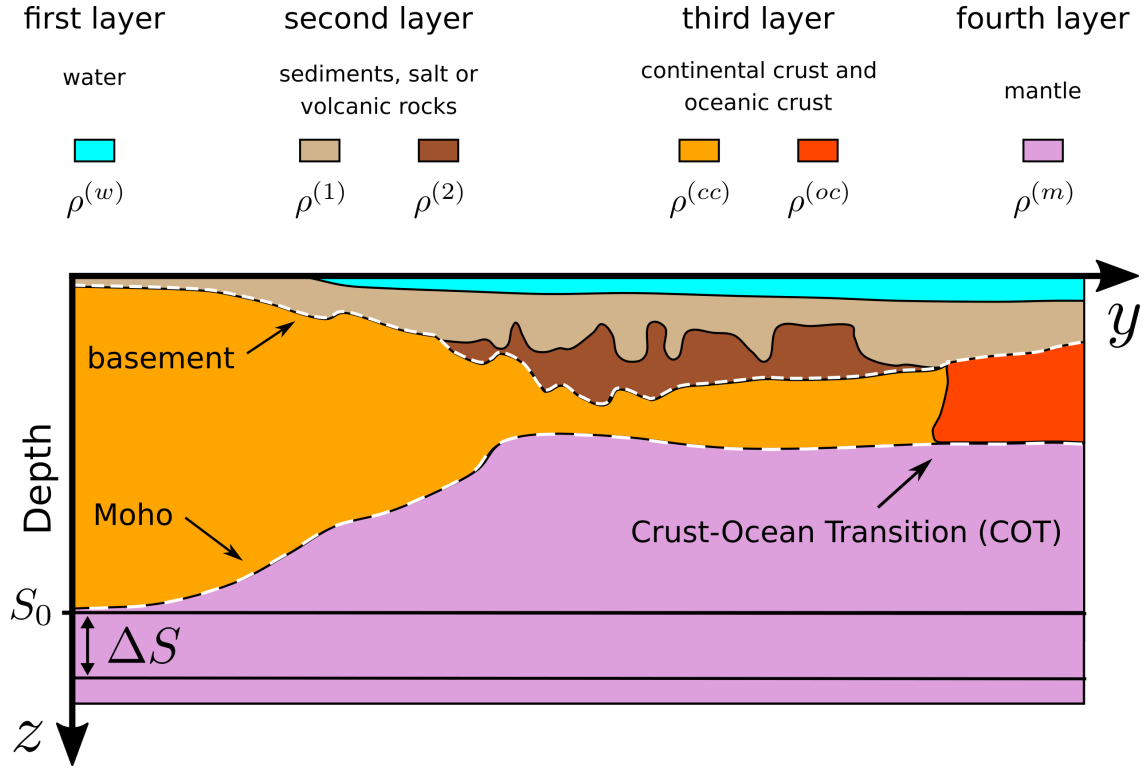


Figure 1: Rifted margin model formed by four layers. The first one represents a water layer with constant density $\rho^{(w)}$. The second layer is formed by Q vertically adjacent parts, according to the geological are to be studied. In this example, $Q = 2$. These parts represent sediments, salt or volcanic rocks and have constant densities $\rho^{(q)}$, $q = 1, \dots, Q$. The third layer represents the crust, which is divided into the continental crust, with a constant density $\rho^{(cc)}$, and the oceanic crust, with a constant density $\rho^{(oc)}$. We presume an abrupt Crust-Ocean Transition (COT). Finally, the fourth layer of our model represents a homogeneous mantle with constant density $\rho^{(m)}$. Basement and Moho are represented by the dashed-white lines. The continuous white lines represent the isostatic compensation depth at S_0 and the reference Moho at $S_0 + \Delta S$.

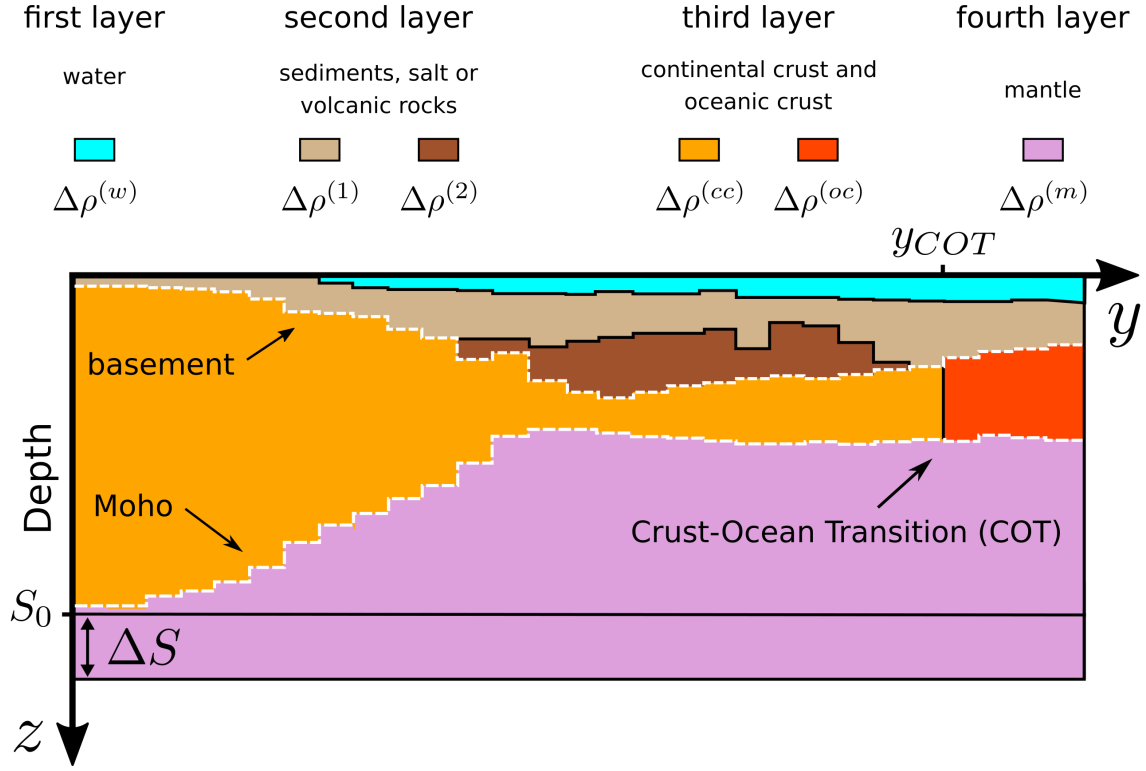


Figure 2: Interpretation model formed by N columns of vertically stacked prisms. Each column is formed by four layers of prisms and locally approximates the four layers of the rifted margin model (Figure 1). Each prism has a constant density contrast defined as the difference between its corresponding density at the rifted margin model (Figure 1) and the constant density $\rho^{(r)}$ of the shallowest layer forming the reference density distribution (see text). Basement and Moho are represented by the dashed-white lines. The continuous white line represents the isostatic compensation depth at S_0 . The base of the interpretation model coincides with the reference Moho located at $S_0 + \Delta S$.

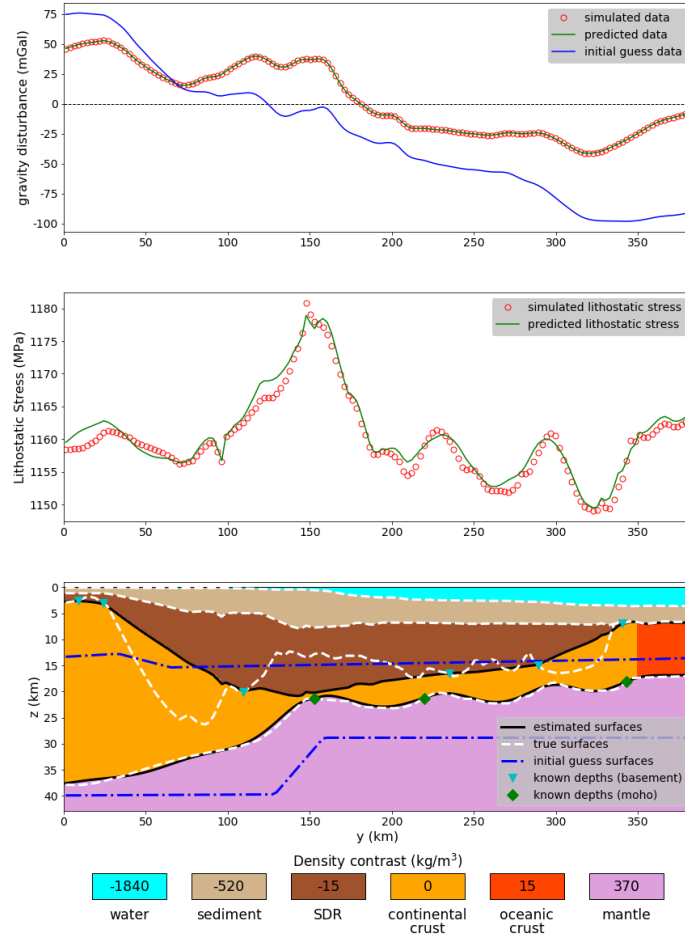


Figure 3: Application to synthetic data. Results obtained in Step 1. (Bottom panel) Estimated and true surfaces, the initial basement and Moho used in the inversion, as well as the known depths at basement and Moho. (Middle panel) True and estimated lithostatic stress curves computed by using equation 6. The values are multiplied by a constant gravity value equal to 9.81 m/s^2 . (Upper panel) True gravity disturbance data produced by the volcanic margin model (simulated data), data produced by the estimated model (predicted data) and data produced the by model used as initial guess in the inversion (initial guess data). The contour of the prisms forming the interpretation model were omitted. The density contrasts were defined according to Table 1.

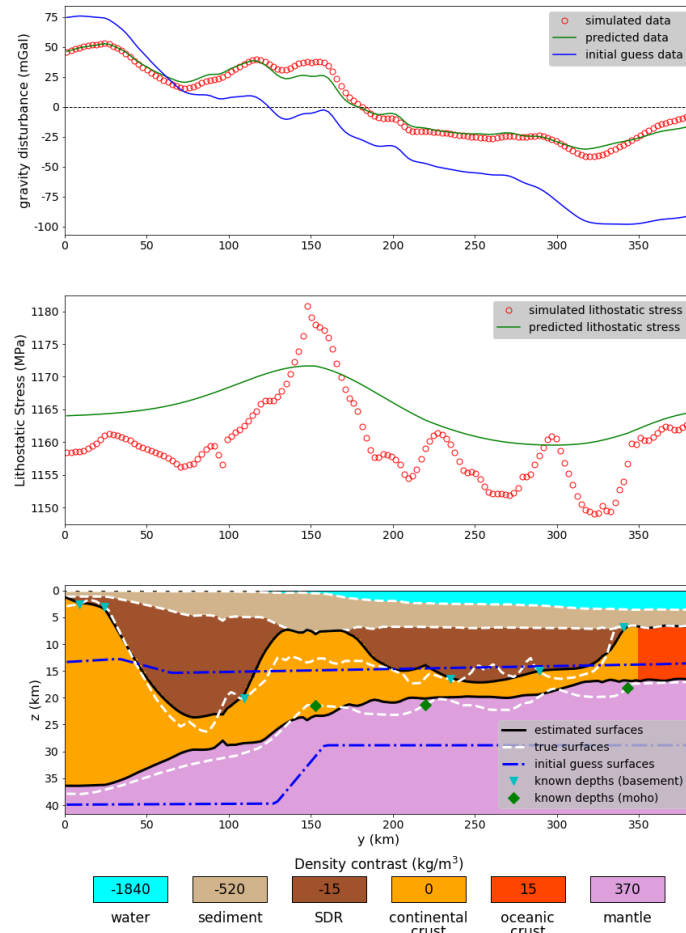


Figure 4: Application to synthetic data. Results obtained in Step 2. The remaining informations are the same shown in the caption of Figure 3.

Bastos and Oliveira Jr. – GEO-XXXX

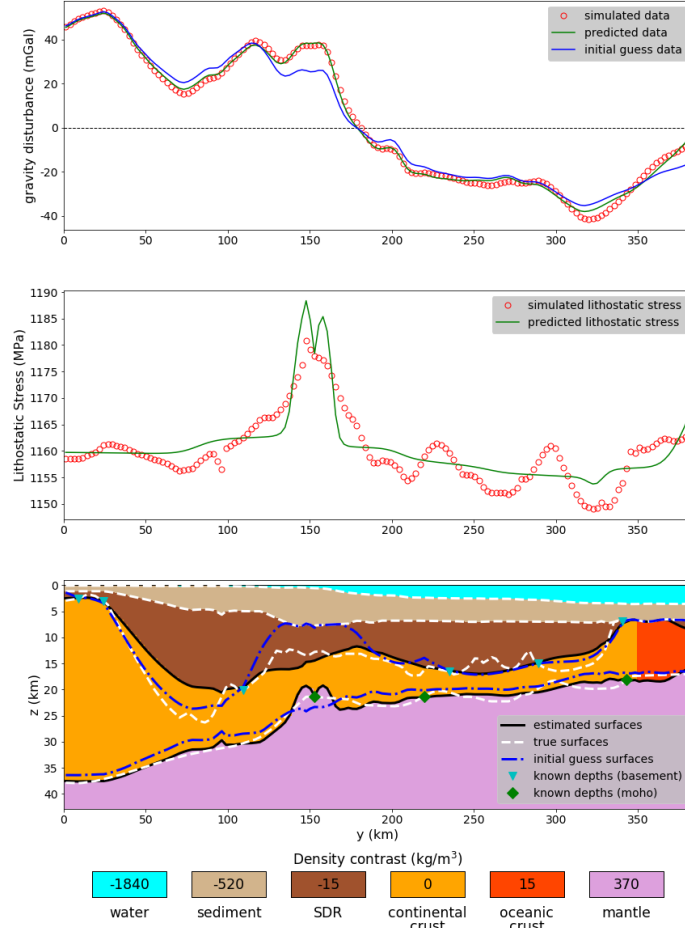


Figure 5: Application to synthetic data. Results obtained in Step 3 by using $\sigma = 21$ (equation 20). The remaining informations are the same shown in the caption of Figure 3.

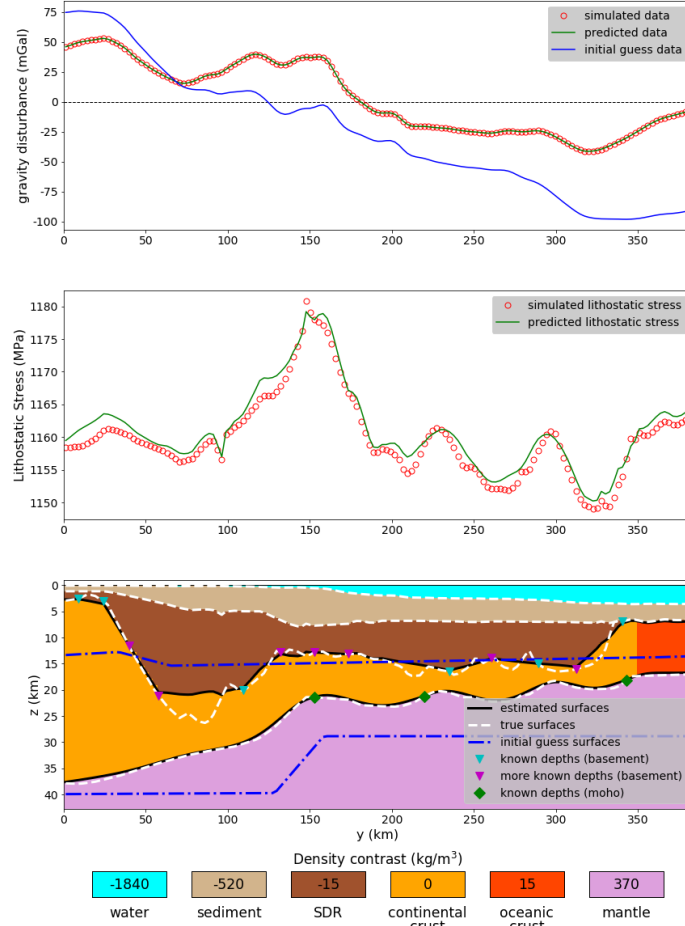


Figure 6: Application to synthetic data. Results obtained in Step 1 by using additional known depths at basement (purple symbols). The remaining informations are the same shown in the caption of Figure 3.

Bastos and Oliveira Jr. – GEO-XXXX

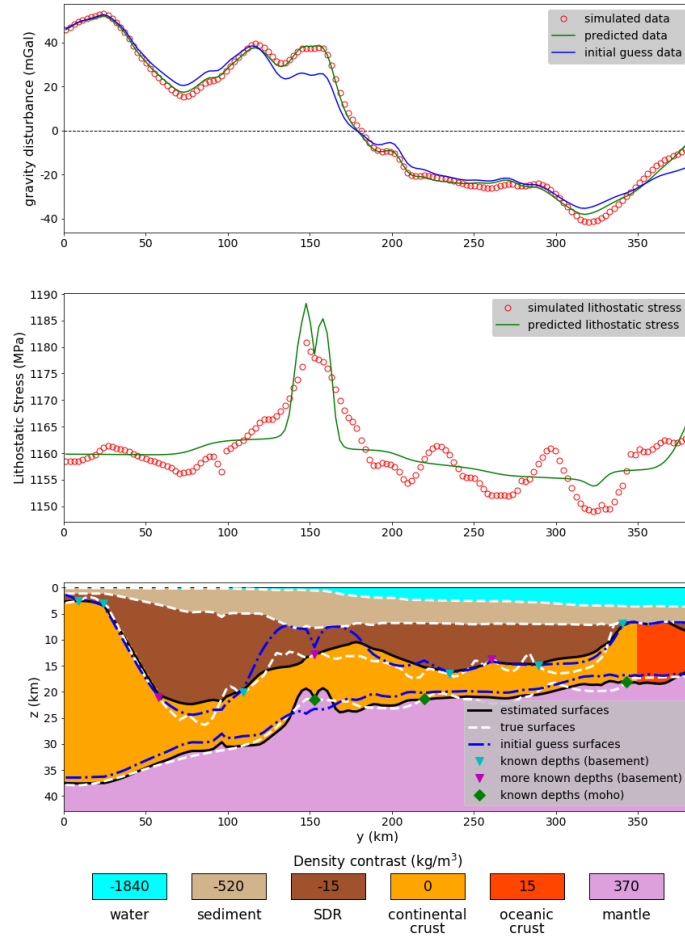


Figure 7: Application to synthetic data. Results obtained in Step 3 by using $\sigma = 21$ (equation 20) and additional known depths at basement (purple symbols). The remaining informations are the same shown in the caption of Figure 3. Notice that, in comparison with the estimated model shown in Figure 6, the number of additional known depths is small.

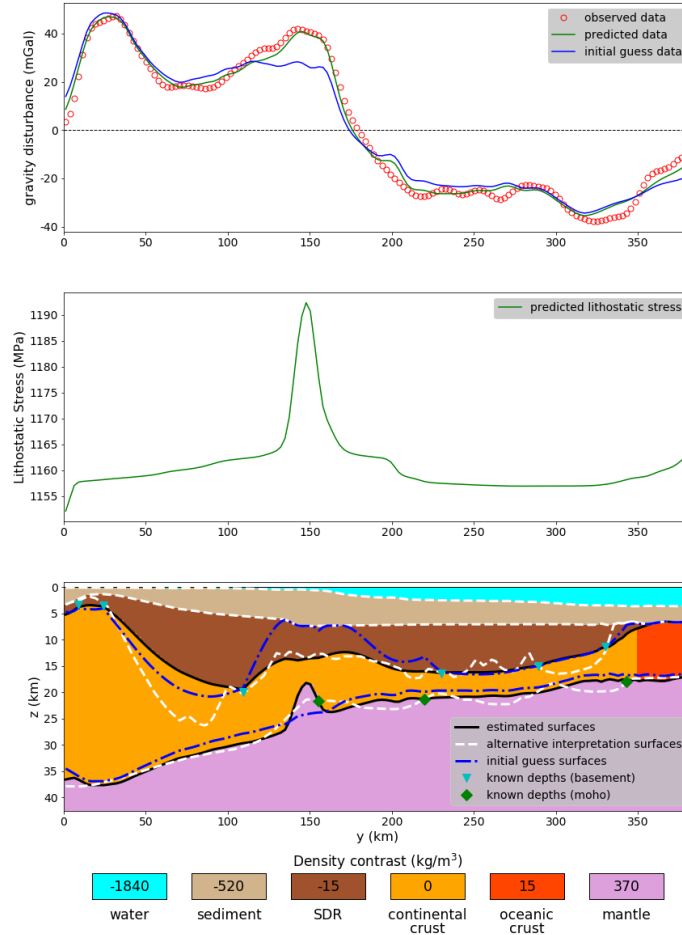


Figure 8: Application to real data on Pelotas basin, Brazil. Results obtained in Step 3 by using $\sigma = 58$ (equation 20). (Bottom panel) Estimated surfaces, initial basement and Moho used in the inversion, as well as the known depths at basement and Moho. The dashed white lines represent an alternative interpretation obtained by Zalán (2015) at the same study area. (Middle panel) Estimated lithostatic stress curve computed by using equation 6. The values are multiplied by a constant gravity value equal to 9.81 m/s^2 . (Upper panel) Observed gravity disturbance data, data produced by the estimated model (predicted data) and data produced the by model used as initial guess in the inversion (initial guess data). The contour of the prisms forming the interpretation model were omitted. The density contrasts were defined according to Table 1.

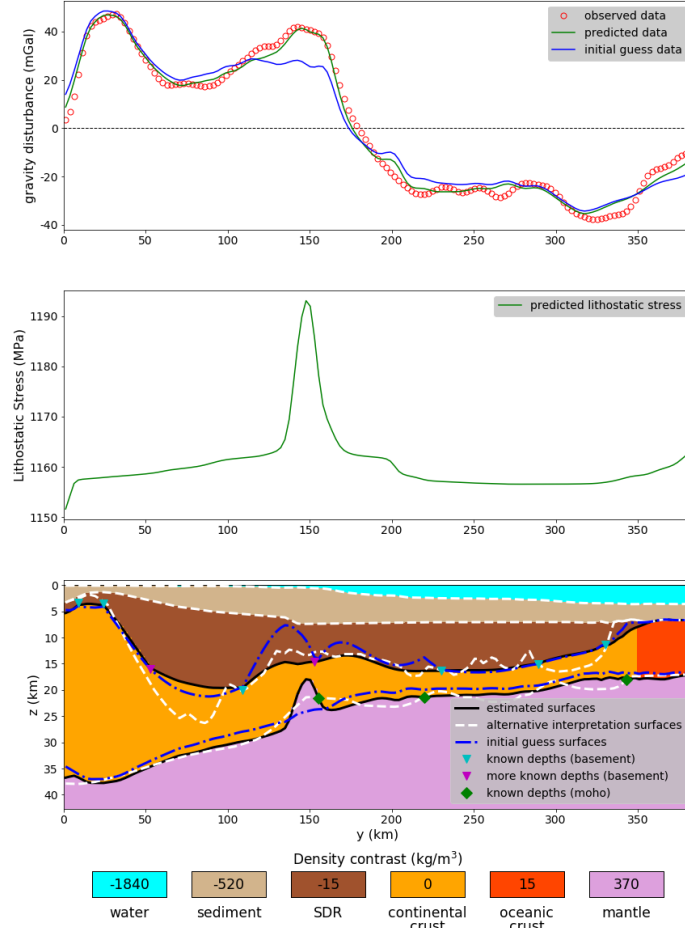


Figure 9: Application to real data on Pelotas basin, Brazil. Results obtained in Step 3 by using $\sigma = 58$ (equation 20) and additional known depths at basement. The remaining informations are the same shown in the caption of Figure 8.

Bastos and Oliveira Jr. – GEO-XXXX